Repulsive electrostatic interactions modulate dense and dilute phase properties of biomolecular condensates

Michael D. Crabtree, Jack Holland, Purnima Kompella, Leon Babl, Noah Turner, Andrew J. Baldwin and Timothy J. Nott

Abstract

Liquid-like membraneless organelles form via multiple, weak interactions between biomolecules. The resulting condensed states constitute novel solvent environments inside eukaryotic cells that partition biomolecules and may favour particular biochemical reactions. Here we demonstrate that, in addition to attractive interactions, repulsive electrostatic interactions modulate condensate properties. We find that net charge modulates the formation, morphology and solvent properties of model Ddx4 condensates in cells and in vitro and that a net negative charge is conserved across germ cell-specific Ddx4 orthologues. This conserved net charge provides a sensitivity to multivalent cations that is not observed in somatic paralogues. The disfavouring effect of a net negative charge in Ddx4 orthologues appears to be offset by increased charge patterning, indicating that fine tuning of both attractive and repulsive interactions can create responsive solvent environments inside biomolecular condensates.

Introduction

Condensation of biomolecules into phase separated bodies provides a reversible way for cells to compartmentalise various processes. Some of these biomolecular condensates are constitutive in eukaryotic cells (1), while others only occur in specific cell types or in response to certain environmental stimuli (2–8). While a condensate may contain hundreds of different components (4), its composition is typically dominated by a small number of major constituents that define the condensate identity and likely control its overall biochemical and biophysical properties (1, 2, 5, 9). These high abundance constituents can be thought of as the basis of the condensate's unique internal solvent environment, into which other (solute) biomolecules may be partitioned. Understanding how the multiple, individually weak interactions made by major components contribute to overall condensate properties is of significant interest.

Various attractive interactions among proteins and nucleic acids have been shown to be important in governing the formation and stability of biomolecular condensates, including cation-pi, pi-pi and charge-charge interactions (9–12). A biomolecule may contain enough of these short-range interaction sites to phase separate on its own (homotypic phase separation), or the interacting groups may come from two different biomolecules. This is apparent in the case of complex coacervation, where at least two oppositely charged polymers are required for phase separation (13).

In addition to attractive interactions, studies on protein aggregation and the stability of colloidal dispersions suggest that repulsive forces also play a significant role in phase separation. For example, electrostatic repulsion between like-charged colloids is required for the long-term stability of dispersions like milk and paints (14, 15), while net charge modulates both the rate and propensity of protein aggregation (16, 17). While significant progress has been made in describing the attractive interactions that promote phase

separation of proteins and nucleic acids into biomolecular condensates, less is known about the role of repulsive forces.

Ddx4 is an essential protein component of biomolecular condensates termed nuage in mammals, P-granules in worms, and pole plasm/polar granules in flies – together referred to as germ granules (18–24). The biological function of germ granules appears to be to house components of a small RNA interference (piRNA) pathway which protects the germline genome against the activity of transposable elements. Structurally, human Ddx4 and its orthologous sequences comprise two intrinsically disordered regions (IDRs) that flank a central DEADbox RNA helicase domain.

We have previously shown that the N-terminal IDR of Ddx4 is sufficient to spontaneously phase separate into condensates both in vitro and in cells (9). A combination of attractive cation-pi interactions between arginine and phenylalanine sidechains, along with patterned electrostatic interactions, stabilise the Ddx4 condensates (9, 25). The solvent environment created inside Ddx4 condensates is able to selectively partition biomolecules from their surroundings and destabilise nucleic acid duplexes (26).

Here, we use the N-terminal region of Ddx4 to investigate the impact of repulsive interactions on the stability and properties of Ddx4 condensates, focussing on net charge. We show that reducing the overall protein net charge, either by mutation or pH, alters the saturation concentration, morphology and solvent properties of Ddx4 condensates, both in vitro and in cells. Strikingly, these properties are found to be sensitive to the divalent cation, Ca^{2+}, in a net charge-dependent manner. We find that sensitivity to calcium is conserved among Ddx4 orthologues, but not somatic paralogues. Analysis of sequence features suggests that Ddx4 orthologues maintain calcium sensitivity through conserving a net negative charge. We propose that repulsive forces between major biomolecular condensate

components can modulate condensate formation, morphology and solvent properties, in

addition to providing sensitivity to external factors such as calcium concentrations.

Results

The saturation concentration of Ddx4 is modulated by net charge

The series of negatively charged residues at the C-terminal region of $Ddx4^N$ provided an opportunity to modulate the net charge through making minimal adjustments to the length of the chain (Figure 1A). Five constructs were produced with predicted net charges at pH 8 spanning from -3.4 (amino acids 1-229) to -7.4 (amino acids 1-238). Importantly, these constructs resulted in a significant titration in net charge, with minimal incremental impact on the total construct length, fraction of charged residues and charge patterning. Using differential interference contrast (DIC) microscopy, we monitored the concentration of each construct that was required to phase separate at 30 ± 1°C as a proxy for droplet stability. For clarity, henceforth we refer to the $Ddx4^N$ construct based on the rounded integer charge at pH 8 e.g. Ddx4 1-236 is referred to as $Ddx4^N(-6)$. Strikingly, compared to our original construct ($Ddx4^N(-6)$), a construct with just one additional charge ($Ddx4^N(-7)$) required 1.5-fold more protein (droplet stability decreased), while a single reduction in net charge ($Ddx4^N(-5)$) led to a 2.8-fold reduction in the concentration of $Ddx4^N$ required (droplet stability increased). As the charge of the construct was reduced further, the concentration of $Ddx4^N$ required to phase separate continued the downward trend (Figure 1B). To confirm that the change in droplet stability was due to the alteration in net charge and not due to a change in specific interactions in the C-terminal region of the protein, we kept the length of the construct constant (1-236) and changed the pH to 6.5. This resulted in a 3-fold reduction in required protein concentration, similar to the 3.7-fold reduction observed for the comparably charged $Ddx4^N(-3)$.

Long-term stability of colloidal dispersions is commonly predicted by estimating the surface charge of the particles within it by measuring their zeta potential (14, 15). The zeta potential is determined by monitoring the speed of movement of particles in an applied electric field via laser doppler velocimetry. As such, particles with higher surface charge move more

quickly in the applied electric field and consequently have a higher zeta potential. In the case of colloidal dispersions, this means that particles with higher zeta potentials have higher surface charges which stabilises the colloidal dispersion due to long-range electrostatic repulsion between like-charged particles. We applied the same technique to the series of Ddx4 constructs and found that reducing the predicted net charge reduced the observed zeta potential, indicating a reduction in apparent surface charge. This reduction in zeta potential was concomitant with favouring phase separation (Figure 1C). Essentially, this can be described as a destabilisation of the dilute phase as the net charge is decreased, as the maximal soluble (dilute phase) protein concentration at a fixed temperature is reduced.

We previously monitored phase separation of Ddx4 in cultured mammalian cells with a YFP-tagged Ddx4 mimic, in which the DEAD-box helicase domain was replaced by YFP (Ddx4^{YFP}) (9). This construct maintained a similar net charge and dimension to full-length Ddx4 (1-724), while permitting visualisation of the protein through YFP fluorescence. Net charge modulation of Ddx4^{YFP} was performed in the same manner as Ddx4^N, creating five constructs with an estimated net charge titration of -8.3 to -12.3 at pH 7.4. Importantly, while the constructs maintained the same change in net charge, the addition of YFP and the C-terminal region of Ddx4^N resulted in these sequence alterations occurring in the middle of protein sequence rather than at one end (Figure 1A). Phase separation was observed for all differently charged Ddx4^{YFP} constructs in HeLa cells (Figure 1D). Consistent with the Ddx4^N data in vitro, an increase in the dense:dilute phase ratio was observed upon reducing the net charge of Ddx4^{YFP} (Figure 1E), indicating a relative destabilisation of the dilute phase.

To understand the decrease in dilute phase stability, we constructed phase diagrams for all Ddx4^N constructs (Figure S1). Entropic and enthalpic contributions to the phase separation were extracted by fitting the data to a Flory-Huggins model, as described previously (9). This indicated that the change in dilute phase stability with reduced net charge was predominantly due to an increased entropic gain upon de-mixing (Figure S1).

Net Charge Modulates Dense Phase Properties of Ddx4 Condensates

Having observed a systematic change in the stability of Ddx4 solutions as a function of protein net charge, we investigated whether the properties of the protein condensates were similarly modulated. The morphology of Ddx4^N droplets sitting on siliconized glass coverslips was visualised using confocal fluorescence microscopy and the fluorescent dye, Alexa 488 as a probe. Increasing the net charge of Ddx4^N caused the condensates to become more beaded, with less of the droplet in contact with the coverslip (Figure 2A). Additionally, Alexa 488 intensity varied for each construct, with the intensity inside of Ddx4^N condensates reducing relative to the outside as the net charge increased (Figure 2B). In contrast, when the protein fluorophore, mCitrine (YFP) was used as a fluorescent probe, YFP intensity inside of Ddx4^N condensates was reduced relative to the outside as the Ddx4^N net charge was decreased. The change in fluorescence intensity ratio can be explained by a change in partitioning of the fluorophore and/or by a change in the fluorescent properties of the fluorophore. As both are dependent on the solvent properties of the dense phase relative to the dilute phase, assuming the dilute phase solvent properties were similar for all constructs, the change in ratio with net charge indicated a change in solvent properties in the Ddx4^N condensates.

To further investigate the impact of net charge on Ddx4 condensates in cells, we utilised the highly charged nature of commonly used, short protein tags (Figure 2C). Importantly, while these tags all modified the net charge of the construct, they all varied in sequence and were cloned at the C-terminus of the construct. Addition of acidic tags resulted in changes in both droplet morphology and dense phase fluorescence intensities (Figure 2D). Ddx4^{YFP} condensates tagged with FLAG and MYC sequences were particularly striking. Rather than the spherical, dense droplets observed for untagged Ddx4^{YFP}, these condensates were less dense and appeared to wet/spread across the nucleoplasm. In contrast, addition of the slightly basic Spot-tag did not lead to significant morphological changes, indicating that the

influence of the acidic tags was due to their impact on net charge, rather than through a disruption of interactions at the C-terminus of the construct.

Ion specific regulation of Ddx4 phase separation

Water purification for sanitation and drinking requires the removal of contaminants and debris. A routine method for promoting aggregation (or flocculation) of particulates is the addition of multivalent ions to the water (27). By adding multivalent ions that are of opposite charge to the contaminants, aggregation is promoted through reducing repulsive interactions between the like-charged particulates. The quantity of multivalent ions required can be estimated through monitoring the zeta potential of the solution, with ions continually added until the zeta potential nears 0. Given the association between net charge, zeta potential and Ddx4 phase separation observed above, we added $CaCl_2$, a salt containing a positively charged divalent ion, into a solution containing droplets composed of negatively charged $Ddx4^N$(-6), and imaged the response in real time. To do this, we required an imaging set up that maintained the sample conditions (e.g. solution volume, protein concentration and pH), but allowed controlled concentrations of $CaCl_2$ to be added at defined timepoints. We achieved this through pipetting a solution of phase separated $Ddx4^N$ droplets onto a siliconized glass coverslip and sealing with a layer of mineral oil. Various solutions could then be pipetted through the oil layer into the solution, with the oil layer resealing upon removal of the pipette tip. Using Alexa 488 as a fluorescent probe as before, the response of $Ddx4^N$ condensates to the addition of $CaCl_2$ was visualised by time-lapse fluorescence confocal microscopy. Before addition of $CaCl_2$, condensates present on the glass surface were beaded and typically <6 μm in diameter (Figure S2). Addition of 10 mM $CaCl_2$ to the solution resulted in rapid (<15 s) changes in morphology. The condensates fused, grew and flattened, wetting the surface of the coverslip. Internal rearrangement was also observed, with regions of dilute phase appearing inside the dense phase condensates. Over a

timescale of minutes, the condensates continued to fuse, forming large (>40 μm) droplets. To confirm that the observed differences were due to the addition of $CaCl_2$, we pipetted ETDA into the solution to chelate the Ca^{2+} ions. The condensates immediately started to shrink and became more beaded, similar to the morphology observed at the start of the experiment. Qualitatively, there also appeared to be a difference in the fluorescence intensity of the droplets with and without $CaCl_2$. We therefore extracted the minimum and maximum pixel intensities and plotted them against time (Figure 3A). This indicated a significant (50%) increase in the maximum pixel intensity after addition of $CaCl_2$, followed by a return to pre-$CaCl_2$ levels after chelating the calcium with EDTA.

To improve the quantitative analysis of the effects of $CaCl_2$ on Ddx4^N condensates, we set up sealed reaction chambers and left phase separated samples to equilibrate for >1 hour before measuring Alexa 488 fluorescence. To control for changes in the ionic strength of the solution, a sample with additional NaCl was also prepared. Consistent with the time-lapse imaging data, samples of Ddx4^N(-6) with $CaCl_2$ had a 50% higher ratio of fluorescence intensity inside the droplet vs outside (Figure 3B). The change in morphology was also confirmed, with $CaCl_2$ samples displaying a more wetted profile (Figure 3C). Furthermore, these effects on the morphology and droplet properties could be tuned by titrating the concentration of $CaCl_2$.

Through monitoring the transition temperature of a constant protein concentration in different solution conditions, we then further investigated how $CaCl_2$ impacted droplet stability. Addition of relatively low (3.3 mM) concentrations of $CaCl_2$ lead to significant increases in the transition temperature (Figure 3D). In contrast, consistent with previous reports that increased ionic strength competes with the attractive cation-pi interactions of Ddx4 condensates (9, 25), addition of NaCl lead to a slight reduction in transition temperature. By repeating the transition temperature experiments at different concentrations of the Ddx4^N(-7) construct, we were able to assess how the entropic and enthalpic contributions altered after

addition of $CaCl_2$. As for the different $Ddx4^N$ constructs, an increase in the entropic term was observed. However, in contrast to the results for the $Ddx4^N$ constructs, stabilisation also occurred through a change in the enthalpic term (Figure S1).

Overall, $CaCl_2$ had a variety of effects on both the dense and dilute phase protein that were reminiscent of altering the net charge of the construct. We therefore measured the zeta potential of the dilute phase and found that $CaCl_2$ reduced the magnitude of the zeta potential in a titratable manner, whereas NaCl addition had no effect (Figure 3E). To investigate whether $CaCl_2$ could impact intracellular Ddx4 phase separation, we expressed $Ddx4^{YFP}$ in Hela cells. Addition of $CaCl_2$ to the culture media resulted in an increase in intracellular calcium levels, and droplet condensation in live cells (Figure S2). Addition of salt to the extracellular media could cause water to leave the cell by osmosis, increasing protein concentrations and consequently Ddx4 phase separation. To confirm that this $CaCl_2$ induced phase separation was not due to this ionic strength effect, we required a high-throughput assay that could determine the percentage of cells containing $Ddx4^{YFP}$ condensates after exposure to different conditions. We therefore developed a flow cytometry protocol, where 50,000 cells could be analysed in minutes. Cells with $Ddx4^{YFP}$ condensates were readily identifiable from a combination of high fluorescence intensity and high fluorescence contrast (Figure S2). Condensate presence in these cells was confirmed by analysis of images taken during flow cytometry. Addition of 10 mM $CaCl_2$ resulted in a 30% increase in the number of cells containing $Ddx4^{YFP}$ condensates, whereas, addition of the same ionic strength of NaCl only lead to a 10% increase, indicating that $CaCl_2$ levels in cells impacted the phase separation of $Ddx4^{YFP}$ beyond the effect seen due to the change in ionic strength (Figure 3F).

Conservation of net charge across Ddx4 homologues

As net charge appeared to be an important modulator of the saturation concentration, morphology and solvent properties of Ddx4 droplets, we decided to investigate the net

charge of Ddx4 orthologues. Averaging the simple net charge (RK-DE) of full-length Ddx4 orthologues from human, mouse, clawed frog, zebrafish, fruit fly and flat worm, gave a mean net charge of -11.7 with a standard deviation of 2.16. In contrast, the somatic paralogues of Ddx4, exemplified by Ddx3x in humans, had an average net charge -1.0 +/- 2.76 (Figure 4A, Figure 4B). A more detailed look at the different sequence domains (IDR1, helicase and IDR2) indicated that the helicase regions of both Ddx3x and Ddx4 orthologues were negatively charged, but, while this charge was compensated by the positively charged disordered regions for Ddx3x, the negatively disordered regions of Ddx4 increased the net negative charge of the sequence (Figure 4A). Interestingly, other sequence features of the full-length proteins appeared to be far more comparable (length: 711 +/- 33 and 706 +/- 50, fraction aromatic residues: 8.25 +/- 0.25 and 8.79 +/- 0.75 each for Ddx4 and Ddx3x orthologues, respectively), suggesting that the difference in net charge between Ddx4 and Ddx3x orthologues may be functionally relevant. We had already identified that the calcium sensitivity of Ddx4^N constructs was related to the magnitude of net negative charge of the sequence (Figure 3B) and therefore wondered if the difference in net charge conserved a sensitivity to calcium across the orthologues. Exposure of the N-terminal disordered region of the fly Ddx4 orthologue, Vasa to $CaCl_2$ increased the transition temperature in a similar manner to human Ddx4. In contrast, the transition temperature of both the human Ddx3x and Ddx3y, and the fly Ddx3x orthologue, Bel, were not significantly altered by $CaCl_2$ addition (Figure 4C).

We previously showed that distribution of charge modulates the phase separation propensity of Ddx4 (9). This charge patterning can be estimated by determining the kappa value for the sequence (28). Interestingly, the patterning of charge for both the N- and C-terminal disordered regions was higher for Ddx4 orthologues compared to the corresponding region in Ddx3x orthologues, indicating that both the patterning and conservation of charge may be important features for Ddx4 function (Figure 4D).

Discussion

Understanding the sequence determinants of biomolecular condensate properties is key to interpreting their function. To form a liquid-like dense compartment, interactions between the biomolecules must be attractive, but of appropriate affinities and time scales to maintain fluidity and prevent hardening. A delicate balance between the valency and patterning of these attractive interactions is therefore required (29). These features are first controlled by the amino acid identity and patterning of the protein sequence produced during translation. Subsequent fine tuning of attractive interactions can occur with post translational modifications. For example, phosphorylation of nephrin enhances phase separation through increasing the valency of attractive interactions with N-WASP (10), whereas methylation of arginine residues reduces the phase separation potential of Ddx4 and FUS through disruption of stabilising cation-pi interactions (9, 30). Here, we have shown that repulsive interactions can similarly impact phase separation both in vitro and in cells. Modulating the net charge of Ddx4 impacted the stability of the dilute phase, and the morphology and solvent properties of the condensed phase. Interestingly, a net negative charge was conserved across Ddx4 orthologues, suggesting that these repulsive interactions are encoded at the genetic level. Given that Ddx4 proteins are required for the formation of phase separated germ granules, this net negative charge would encode repulsive interactions that would typically disfavour their formation. To overcome this, charge distribution in the primary sequence of Ddx4 appears to be more patterned than its less charged, somatic paralogue, Ddx3x.

While NaCl has been shown to inhibit phase separation of Ddx4 through disrupting cation-pi interactions (9, 25), addition of $CaCl_2$ was found to promote phase separation. Although the mechanism for the difference between the two salts is not clear, addition of $CaCl_2$ affected the zeta potential, whereas NaCl did not. The effect of $CaCl_2$ on Ddx4 dilute phase stability, condensate morphology and solvent properties such as partitioning was comparable to reducing the net charge of the Ddx4 protein chain. These effects were rapid, reversible and

could be observed at low concentrations (as low as 3.3 mM $CaCl_2$). Multivalent ions have been shown to influence the phase separation of BSA (31) while calcium has been shown to impact RNA-RNA and RNA-poly arginine peptide coacervates at concentrations above 50 mM (32). Structural calcium binding motifs are typically responsible for high affinity calcium interactions (33), however none of the classical sequences are obviously present in Ddx4. Instead, the response to calcium appeared to be modulated by the net charge of the sequence, with the conserved, net negative charge of Ddx4 promoting calcium sensitivity.

Intriguingly, calcium has been identified in nuage in mouse spermatids (34, 35), and the distributions and amounts of intracellular calcium are known to fluctuate during spermatogenesis (36). Medicative consumption of calcium channel blockers is known to reduce male fertility due to multiple factors, including blocking of spermatogenesis and germ cell maturation (37). A similar outcome is also observed in Ddx4 knockouts: germ cell maturation is blocked (24). Nuage abundance, location and morphology changes throughout spermatogenesis, suggesting that it is under tight regulation and that modulation of nuage is required for appropriate germ cell maturation (38). While further studies are clearly required, it is tempting to suggest that the conserved net negative charge of Ddx4 orthologues may encode an ability to alter the stability, morphology and solvent properties of nuage in response to external stimuli such as calcium concentration. In this regard, calcium would be acting as a post-translational modifier of Ddx4 net charge. A more traditional post-translational modifier of net charge, phosphorylation, is known modulate the stability and partitioning of complex coacervates (39) as well as the stability and morphology of several other proteins (40, 41), while DYRK kinases have been proposed as key modulators of phase separation (42). For models of heterotypic phase separation, these changes in charge have been linked to a change in long-range electrostatic repulsion (43, 44). Using Ddx4 as a model system, we have examined the role of these repulsive electrostatic forces in homotypic protein phase separation and have shown that net charge can modulate biomolecular condensate formation, morphology and solvent properties. Addition of net

charge to the molecular grammar of phase separation (Figure 4F) could help to explain

effects seen after post-translational modification of phase separating proteins, and could aid

in designing synthetic phase separating systems with unique properties.

Acknowledgements

References

1. Lafontaine, D. L. J., Riback, J. A., Bascetin, R., and Brangwynne, C. P. (2020) The nucleolus as a multiphase liquid condensate. *Nat. Rev. Mol. Cell Biol.* 10.1038/s41580-020-0272-6

2. Yang, P., Mathieu, C., Kolaitis, R. M., Zhang, P., Messing, J., Yurtsever, U., Yang, Z., Wu, J., Li, Y., Pan, Q., Yu, J., Martin, E. W., Mittag, T., Kim, H. J., and Taylor, J. P. (2020) G3BP1 Is a Tunable Switch that Triggers Phase Separation to Assemble Stress Granules. *Cell*. **181**, 325-345.e28

3. Dodson, A. E., and Kennedy, S. (2020) Phase Separation in Germ Cells and Development. *Dev. Cell*. **55**, 4–17

4. Stenström, L., Mahdessian, D., Gnann, C., Cesnik, A. J., Ouyang, W., Leonetti, M. D., Uhlén, M., Cuylen-Haering, S., Thul, P. J., and Lundberg, E. (2020) Mapping the nucleolar proteome reveals a spatiotemporal organization related to intrinsic protein disorder. *Mol. Syst. Biol.* 10.15252/msb.20209469

5. Feric, M., Vaidya, N., Harmon, T. S., Mitrea, D. M., Zhu, L., Richardson, T. M., Kriwacki, R. W., Pappu, R. V., and Brangwynne, C. P. (2016) Coexisting Liquid Phases Underlie Nucleolar Subcompartments. *Cell*. **165**, 1686–1697

6. Jain, S., Wheeler, J. R., Walters, R. W., Agrawal, A., Barsic, A., and Parker, R. (2016) ATPase-Modulated Stress Granules Contain a Diverse Proteome and Substructure. *Cell*. **164**, 487–498

7. Hagai, M.-K., Siany, A., Kedersha, N., Knafo, N., Rivkin, N., Danino, Y., Cohen, N., Olender, T., Moens, T., Higginbottom, A., Cooper-Knock, J., Eitan, C., Toth Cohen, B., Van Den Bocho, L., Anderson, P., Ivanov, P., Geiger, T., and Hornstein, E. (2020) Spatio-temporal Proteomic Analysis of Stress Granule disassembly using APEX Reveals Regulation by SUMOylation and links to ALS pathogenesis. *bioRxiv*. 10.1101/2020.01.29.830133

8. Han, T. W., Kato, M., Xie, S., Wu, L. C., Mirzaei, H., Pei, J., Chen, M., Xie, Y., Allen,

J., Xiao, G., and McKnight, S. L. (2012) Cell-free formation of RNA granules: Bound RNAs identify features and components of cellular assemblies. *Cell*. **149**, 768–779

9.   Nott, T. J., Petsalaki, E., Farber, P., Jervis, D., Fussner, E., Plochowietz, A., Craggs, T. D., Bazett-Jones, D. P., Pawson, T., Forman-Kay, J. D., and Baldwin, A. J. (2015) Phase Transition of a Disordered Nuage Protein Generates Environmentally Responsive Membraneless Organelles. *Mol. Cell*. **57**, 936–947

10. Li, P., Banjade, S., Cheng, H.-C., Kim, S., Chen, B., Guo, L., Llaguno, M., Hollingsworth, J. V., King, D. S., Banani, S. F., Russo, P. S., Jiang, Q.-X., Nixon, B. T., and Rosen, M. K. (2012) Phase transitions in the assembly of multivalent signalling proteins. *Nature*. **483**, 336–340

11. Wang, J., Choi, J.-M., Holehouse, A. S., Lee, H. O., Zhang, X., Jahnel, M., Maharana, S., Lemaitre, R., Pozniakovsky, A., Drechsel, D., Poser, I., Pappu, R. V., Alberti, S., and Hyman, A. A. (2018) A Molecular Grammar Governing the Driving Forces for Phase Separation of Prion-like RNA Binding Proteins. *Cell*. **174**, 1–12

12. Vernon, R. M. C., Chong, P. A., Tsang, B., Kim, T. H., Bah, A., Farber, P., Lin, H., and Forman-Kay, J. D. (2018) Pi-Pi contacts are an overlooked protein feature relevant to phase separation. *Elife*. 10.7554/eLife.31486

13. Sing, C. E., and Perry, S. L. (2020) Recent progress in the science of complex coacervation. *Soft Matter*. **16**, 2885–2914

14. Tholstrup Sejersen, M., Salomonsen, T., Ipsen, R., Clark, R., Rolin, C., and Balling Engelsen, S. (2007) Zeta potential of pectin-stabilised casein aggregates in acidified milk drinks. *Int. Dairy J.* **17**, 302–307

15. Fujitani, T. (1996) Stability of pigment and resin dispersions in waterborne paint. *Prog. Org. Coatings.* **29**, 97–105

16. Tedeschi, G., Mangiagalli, M., Chmielewska, S., Lotti, M., Natalello, A., and Brocca, S. (2017) Aggregation properties of a disordered protein are tunable by pH and depend on its net charge per residue. *Biochim. Biophys. Acta - Gen. Subj.* **1861**, 2543–2550

17.   Zapadka, K. L., Becher, F. J., Gomes dos Santos, A. L., and Jackson, S. E. (2017) Factors affecting the physical stability (aggregation) of peptide therapeutics. *Interface Focus*. 10.1098/rsfs.2017.0030

18.   Castrillon, D. H., Quade, B. J., Wang, T. Y., Quigley, C., and Crum, C. P. (2000) The human VASA gene is specifically expressed in the germ cell lineage. *Proc. Natl. Acad. Sci. U. S. A.* **97**, 9585–9590

19.   Schüpbach, T., and Wieschaus, E. (1986) Maternal-effect mutations altering the anterior-posterior pattern of the Drosophila embryo. *Roux's Arch. Dev. Biol.* **195**, 302–317

20.   Spike, C., Meyer, N., Racen, E., Orsborn, A., Kirchner, J., Kuznicki, K., Yee, C., Bennett, K., and Strome, S. (2008) Genetic analysis of the Caenorhabditis elegans GLH family of P-granule proteins. *Genetics*. **178**, 1973–1987

21.   Kotaja, N., and Sassone-Corsi, P. (2007) The chromatoid body: a germ-cell-specific RNA-processing centre. *Nat. Rev. Mol. Cell Biol.* **8**, 85–90

22.   Breitwieser, W., Markussen, F. H., Horstmann, H., and Ephrussi, A. (1996) Oskar protein interaction with vasa represents an essential step in polar granule assembly. *Genes Dev.* **10**, 2179–2188

23.   Kirino, Y., Vourekas, A., Kim, N., De Lima Alves, F., Rappsilber, J., Klein, P. S., Jongens, T. A., and Mourelatos, Z. (2010) Arginine methylation of vasa protein is conserved across phyla. *J. Biol. Chem.* **285**, 8148–8154

24.   Raz, E. (2000) The function and regulation of vasa-like genes in germ-cell development. *Genome Biol.* **1**, reviews1017.1

25.   Brady, J. P., Farber, P. J., Sekhar, A., Lin, Y. H., Huang, R., Bah, A., Nott, T. J., Chan, H. S., Baldwin, A. J., Forman-Kay, J. D., and Kay, L. E. (2017) Structural and hydrodynamic properties of an intrinsically disordered region of a germ cell-specific protein on phase separation. *Proc. Natl. Acad. Sci. U. S. A.* **114**, E8194–E8203

26.   Nott, T. J., Craggs, T. D., and Baldwin, A. J. (2016) Membraneless organelles can melt nucleic acid duplexes and act as biomolecular filters. *Nat. Chem.* **8**, 569–575

27. Henderson, R. K., Parsons, S. A., and Jefferson, B. (2008) Successful Removal of Algae through the Control of Zeta Potential. *Sep. Sci. Technol.* **43**, 1653–1666

28. Das, R. K., and Pappu, R. V (2013) Conformations of intrinsically disordered proteins are influenced by linear sequence distributions of oppositely charged residues. *Proc. Natl. Acad. Sci.* **110**, 13392–13397

29. Martin, E. W., Holehouse, A. S., Peran, I., Farag, M., Incicco, J. J., Bremer, A., Grace, C. R., Soranno, A., Pappu, R. V., and Mittag, T. (2020) Valence and patterning of aromatic residues determine the phase behavior of prion-like domains. *Science.* **367**, 694–699

30. Qamar, S., Wang, G. Z., Randle, S. J., Ruggeri, F. S., Varela, J. A., Lin, J. Q., Phillips, E. C., Miyashita, A., Williams, D., Ströhl, F., Meadows, W., Ferry, R., Dardov, V. J., Tartaglia, G. G., Farrer, L. A., Kaminski Schierle, G. S., Kaminski, C. F., Holt, C. E., Fraser, P. E., Schmitt-Ulms, G., Klenerman, D., Knowles, T., Vendruscolo, M., and St George-Hyslop, P. (2018) FUS Phase Separation Is Modulated by a Molecular Chaperone and Methylation of Arginine Cation-π Interactions. *Cell.* **173**, 720-734.e15

31. Matsarskaia, O., Roosen-Runge, F., Lotze, G., Möller, J., Mariani, A., Zhang, F., and Schreiber, F. (2018) Tuning phase transitions of aqueous protein solutions by multivalent cations. *Phys. Chem. Chem. Phys.* **20**, 27214–27225

32. Onuchic, P. L., Milin, A. N., Alshareedah, I., Deniz, A. A., and Banerjee, P. R. (2019) Divalent cations can control a switch-like behavior in heterotypic and homotypic RNA coacervates. *Sci. Rep.* **9**, 1–10

33. Rigden, D. J., and Galperin, M. Y. (2004) The DxDxDG motif for calcium binding: Multiple structural contexts and implications for evolution. *J. Mol. Biol.* **343**, 971–984

34. Andonov, M. D., and Chaldakov, G. N. (1989) Morphological evidence for calcium storage in the chromatoid body of rat spermatids. *Experientia*. **45**, 377–378

35. Rouelle-Rossier, V. B., Biggiogera, M., and Fakan, S. (1993) Ultrastructural detection of calcium and magnesium in the chromatoid body of mouse spermatids by electron spectroscopic imaging and electron energy loss spectroscopy. *J. Histochem.*

Cytochem. **41**, 1155–1162

36.   Golpour, A., Pšenička, M., and Niksirat, H. (2016) Ultrastructural Localization of Intracellular Calcium During Spermatogenesis of Sterlet (Acipenser ruthenus). *Microsc. Microanal.* **22**, 1155–1161

37.   Lee, J. H., Ahn, H. J., Lee, S. J., Gye, M. C., and Min, C. K. (2011) Effects of L- and T-type Ca2+ channel blockers on spermatogenesis and steroidogenesis in the prepubertal mouse testis. *J. Assist. Reprod. Genet.* **28**, 23–30

38.   Voronina, E., Seydoux, G., Sassone-Corsi, P., and Nagamori, I. (2011) RNA granules in germ cells. *Cold Spring Harb. Perspect. Biol.* **3**, a002774

39.   Aumiller, W. M., and Keating, C. D. (2016) Phosphorylation-mediated RNA/peptide complex coacervation as a model for intracellular liquid organelles. *Nat. Chem.* **8**, 129–137

40.   Ambadipudi, S., Biernat, J., Riedel, D., Mandelkow, E., and Zweckstetter, M. (2017) Liquid–liquid phase separation of the microtubule-binding repeats of the Alzheimer-related protein Tau. *Nat. Commun.* **8**, 275

41.   Monahan, Z., Ryan, V. H., Janke, A. M., Burke, K. A., Rhoads, S. N., Zerze, G. H., O'Meally, R., Dignon, G. L., Conicella, A. E., Zheng, W., Best, R. B., Cole, R. N., Mittal, J., Shewmaker, F., and Fawzi, N. L. (2017) Phosphorylation of the FUS low-complexity domain disrupts phase separation, aggregation, and toxicity. *EMBO J.* **36**, 2951–2967

42.   Rai, A. K., Chen, J.-X., Selbach, M., and Pelkmans, L. (2018) Kinase-controlled phase transition of membraneless organelles in mitosis. *Nature.* **559**, 211–216

43.   Kim, T. H., Tsang, B., Vernon, R. M., Sonenberg, N., Kay, L. E., and Forman-Kay, J. D. (2019) Phospho-dependent phase separation of FMRP and CAPRIN1 recapitulates regulation of translation and deadenylation. *Science.* 10.1126/science.aax4240

44.   Alshareedah, I., Kaur, T., Ngo, J., Seppala, H., Kounatse, L.-A. D., Wang, W., Moosa, M. M., and Banerjee, P. R. (2019) Interplay between Short-Range Attraction and

Long-Range Repulsion Controls Reentrant Liquid Condensation of Ribonucleoprotein–RNA Complexes. *J. Am. Chem. Soc.* **141**, 14593–14602

45.   Holehouse, A. S., Das, R. K., Ahad, J. N., Richardson, M. O. G., and Pappu, R. V. (2017) CIDER: Resources to Analyze Sequence-Ensemble Relationships of Intrinsically Disordered Proteins. *Biophys. J.* **112**, 16–21

46.   Holland, J., Crabtree, M. D., and Nott, T. J. (2020) In vitro transition temperature measurement of phase-separating proteins by microscopy. in *Methods in Molecular Biology*, pp. 703–714, Humana Press Inc., **2141**, 703–714

47.   Schindelin, J., Arganda-Carreras, I., Frise, E., Kaynig, V., Longair, M., Pietzsch, T., Preibisch, S., Rueden, C., Saalfeld, S., Schmid, B., Tinevez, J. Y., White, D. J., Hartenstein, V., Eliceiri, K., Tomancak, P., and Cardona, A. (2012) Fiji: An open-source platform for biological-image analysis. *Nat. Methods*. **9**, 676–682

48.   Goldberg, I. G., Allan, C., Burel, J. M., Creager, D., Falconi, A., Hochheiser, H., Johnston, J., Mellen, J., Sorger, P. K., and Swedlow, J. R. (2005) The Open Microscopy Environment (OME) Data Model and XML file: open tools for informatics and quantitative analysis in biological imaging. *Genome Biol.* **6**, R47

49.   Consortium, T. U. (2019) UniProt: A worldwide hub of protein knowledge. *Nucleic Acids Res.* **47**, D506–D515

50.   Waterhouse, A. M., Procter, J. B., Martin, D. M. A., Clamp, M., and Barton, G. J. (2009) Jalview Version 2-A multiple sequence alignment editor and analysis workbench. *Bioinformatics*. **25**, 1189–1191
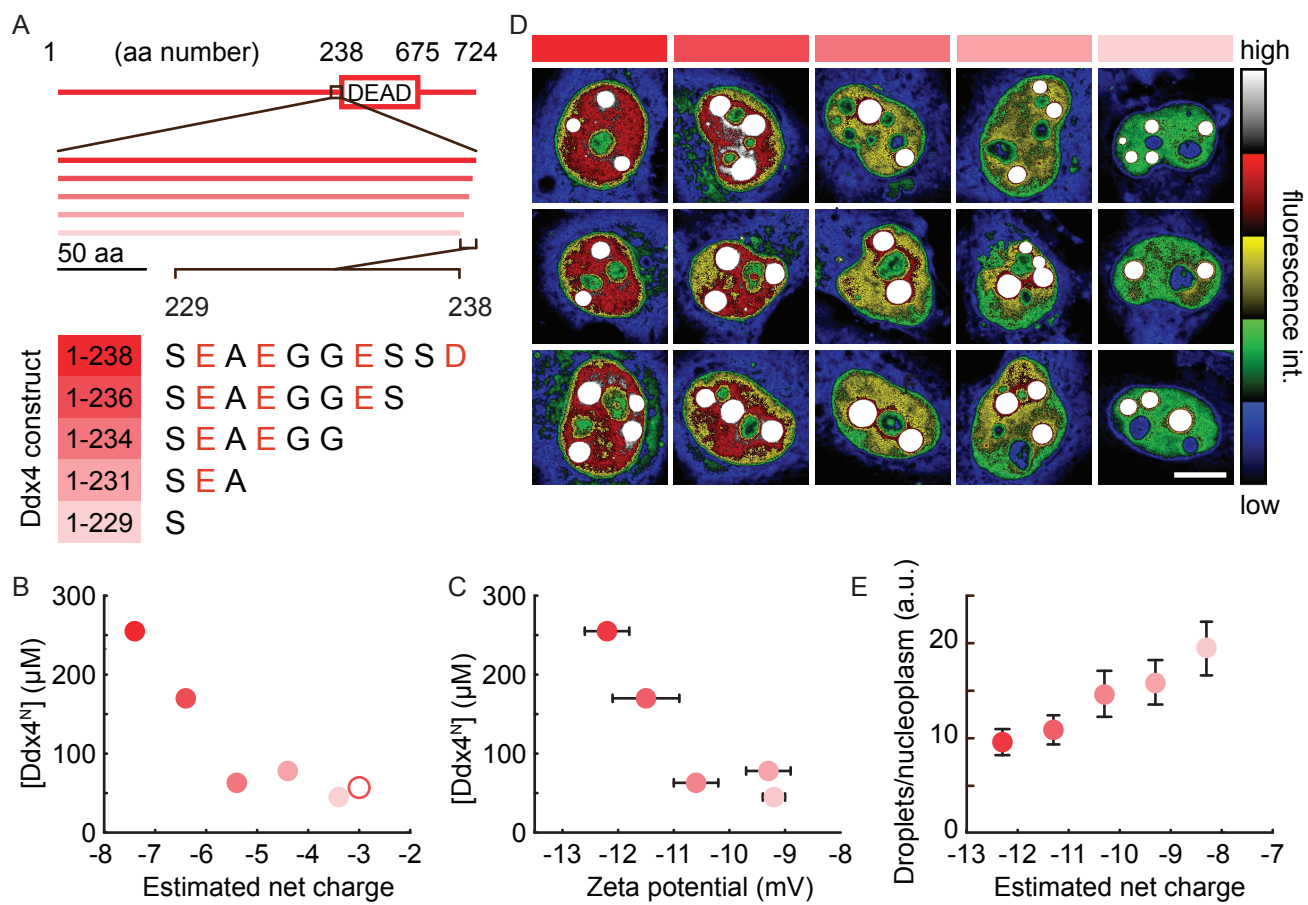
Figure 1

Figure 1. Net charge modulates the in vitro and in cell phase separation propensity of Ddx4.

(A) A series of negatively charged residues occur at the boundary between the N-terminal intrinsically disordered region (line) and folded helicase domain (rectangle) of Ddx4. Small changes to the length of the N-terminal Ddx4^N construct therefore produce significant changes in net charge. Negative charge is indicated in red, with the intensity change illustrating the relative reduction in the magnitude of the net negative charge for Ddx4^N 1-238 to 1-229 constructs. (B) The protein concentration required to phase separate at 30 ± 1 °C decreased as the estimated net charge of the construct was reduced either by pH (open circle) or mutation, indicating a relative destabilisation of the dilute phase. Estimated net charges were computed at pH 8 using pKa values for ionisable groups and the Henderson-Hasselbalch equation, as described in the materials and methods. (C) The change in zeta potential for the different constructs confirmed that the difference in dilute phase stability was due to a change in apparent surface charge. Error bars represent the standard error of the mean (N = 2-3). (D) Ddx4 constructs with the DEAD-box helicase domain replaced with YFP (Ddx4^{YFP}) showed changes in dilute phase intensity when expressed in Hela cells as the net charge was reduced. Scale bar 10 μm. (E) An increase in the dense/dilute (droplet/nucleoplasm) ratio was observed as the net charge of the Ddx4^{YFP} constructs was reduced, indicating a relative destabilisation of the dilute phase. Net charges calculated as in B. Error bars represent the standard deviation.
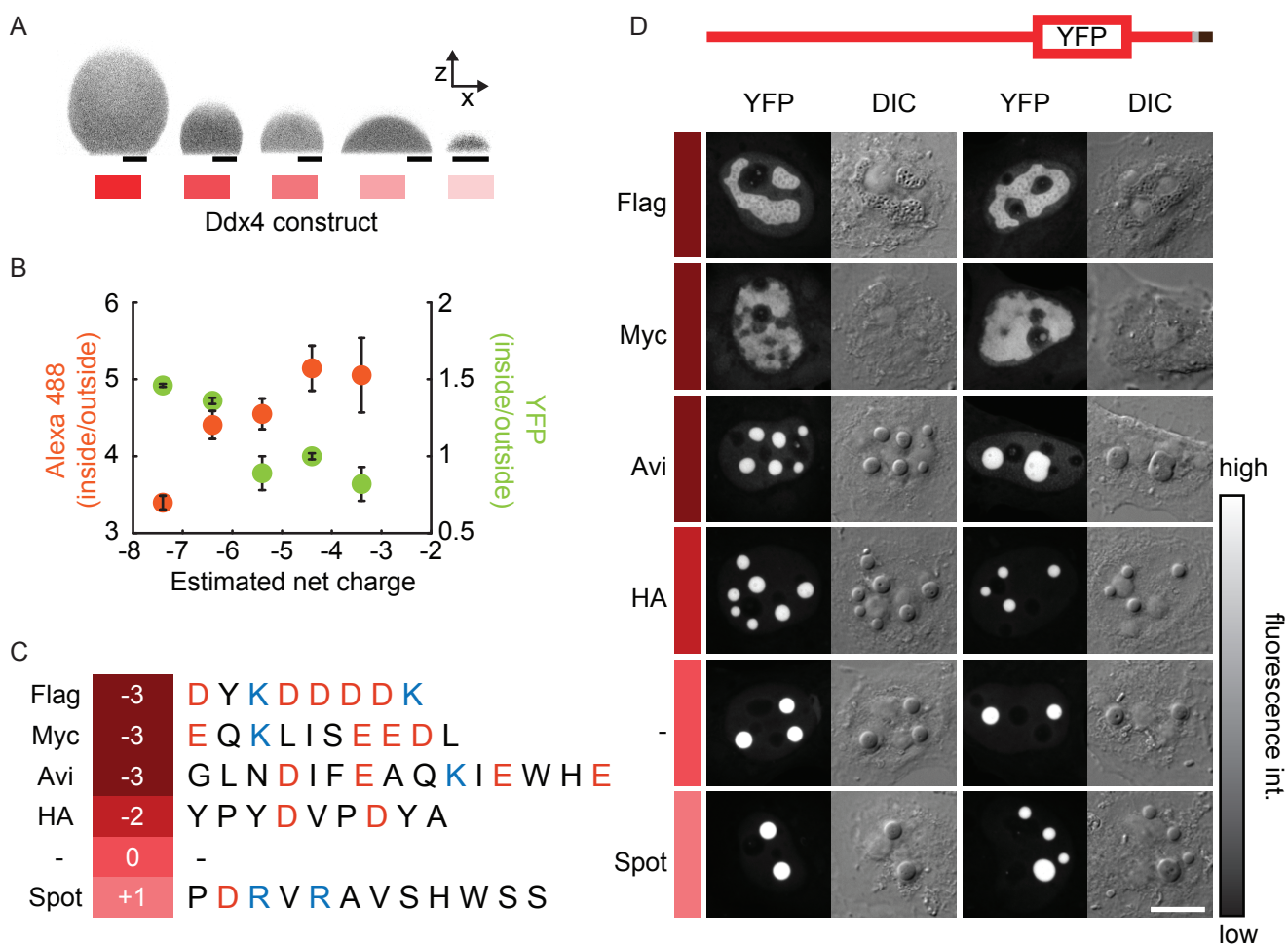
Figure 2

Figure 2. Net charge modulates the dense phase properties of Ddx4 condensates in vitro and in cells.

(A) Ddx4^N constructs displayed varying morphologies on siliconized glass coverslips, with a reduction in net charge leading to smaller, more wetted droplets. Contrast was achieved with the addition of 0.6 µM Alexa 488. Negative charge is indicated in red, with the intensity change illustrating the relative reduction in the magnitude of the net negative charge for Ddx4^N. Scale bars 5 µm. (B) The ratio of fluorescence intensity between the inside and outside of the Ddx4^N condensates varied depending on the net charge of the construct. Alexa 488 (orange circles) had a greater ratio at low net charges, whereas YFP (green circles) had an increased ratio at high net charges. Error bars represent the standard deviation. (C) The net charge of Ddx4^{YFP} was modified by addition of common, short peptide tags at the extreme C-terminus of the construct. Numbers indicate the net charge of the tag based on the number of acidic amino acids (ED, blue) subtracted from the number of positively charged amino acids (RK, red). (D) A change in morphology and dense phase intensity was observed for the negatively charged Flag and Myc tags. The black section in the schematic, top, indicates the position of the tag. Grey section refers to a GSGSG linker. Scale bar 10 µm.
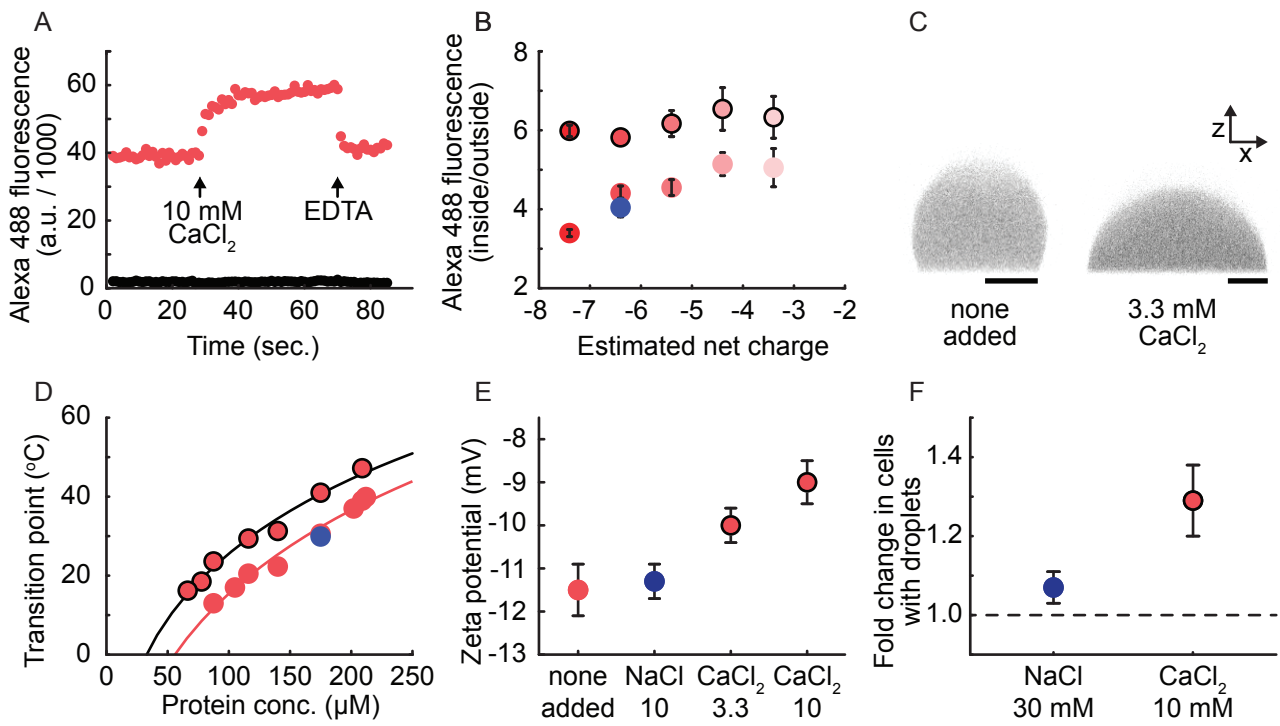
Figure 3

Figure 3. Calcium alters the stability, morphology and solvent properties of Ddx4 condensates.

(A) Addition of 10 mM $CaCl_2$ to Ddx4^N(-6) condensates resulted in a rapid change in dense phase Alexa 488 intensity, which was reversed upon addition of EDTA. The data points represent the minimum (black) and maximum (red) fluorescence intensity in the field of view, with the maximum and minimum values used as proxies for changes Alexa 488 fluorescence intensity in the dense and dilute phase, respectively. (B) As the charge of Ddx4^N constructs was reduced, the addition of 10 mM $CaCl_2$ (bold edges circles) had less of an impact on the dense/dilute phase intensity ratio of Alexa 488 fluorescence. Error bars represent the standard deviation. Blue data point indicates 30 mM addition of NaCl. (C) Addition of 10 mM $CaCl_2$ resulted in Ddx4^N(-6) droplets displaying a more wetted profile when sat on siliconized glass coverslips. Scale bar 5 μm. (D) Addition of 3.3 mM $CaCl_2$ (bold edged circles) destabilised the dilute phase of Ddx4^N(-6), resulting in an upwards shift in the phase diagram. Blue data point indicates 10 mM addition of NaCl. (E) The apparent surface charge of Ddx4^N(-6) was reduced upon $CaCl_2$ addition, but not by an equivalent ionic strength of NaCl, as shown by the reduction in magnitude of the zeta potential. Error bars represent the standard error of the mean (N = 3-4). (F) Flow cytometry confirmed that addition of $CaCl_2$ to the media of HeLa cells transiently transfected with Ddx4^{YFP} increased the number of cells with droplets, beyond the effect observed due to the change in ionic strength. Data are shown as a fold change relative to the number of cells with droplets in the background buffer (20 mM Hepes, 137 mM NaCl, 2.7 mM KCl, pH 7.4). Error bars represent the standard error of the mean.
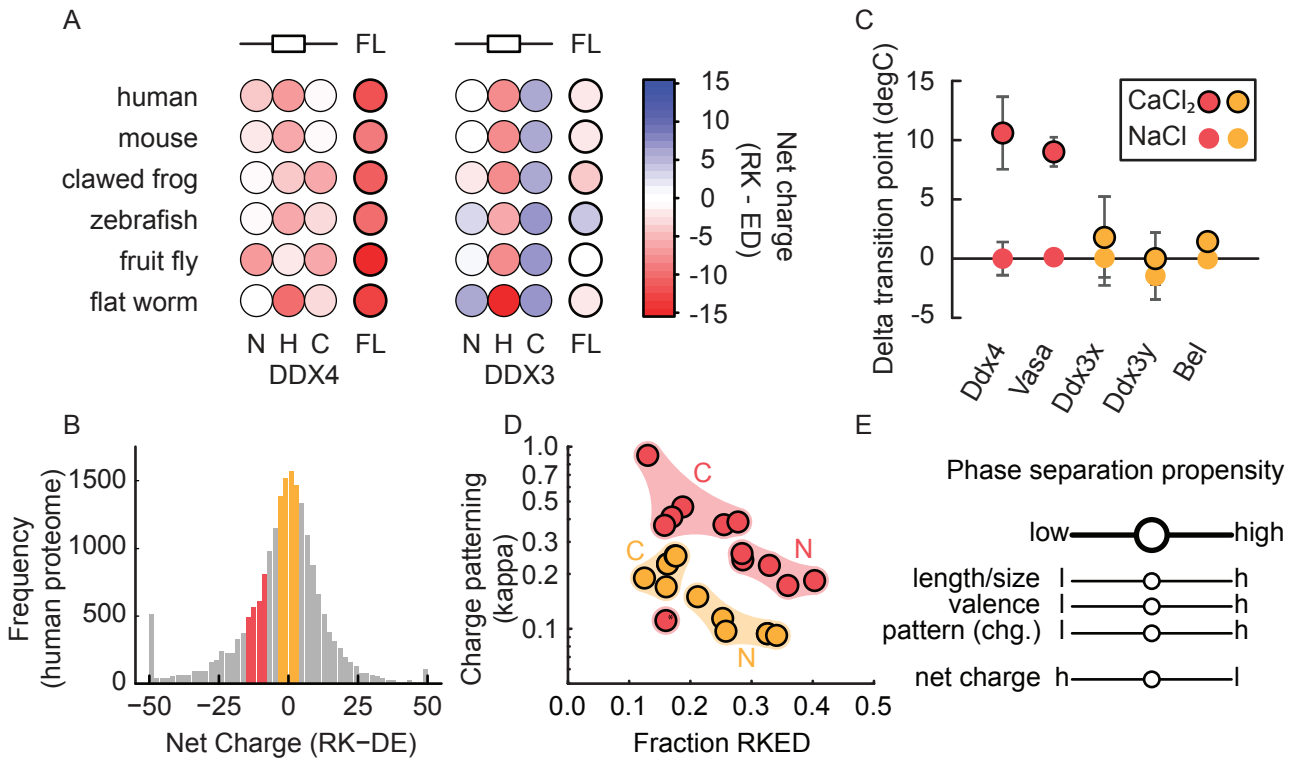
Figure 4

Figure 4. Conservation of net charge among Ddx4 orthologues.

(A) Indicated full-length (FL) Ddx4 orthologues all have a net negative charge. In contrast, whilst the folded helicase domain of Ddx3x had a net charge comparable to Ddx4, the N- and C-terminal disordered regions were typically neutral or positively charged, resulting the full-length net charge for Ddx3x orthologues being close to neutral. The folded helicase domain is represented by a rectangle (middle of three circles), disordered regions by lines (N- and C-terminal regions as the 1st and 3rd of the three circles). The colour map indicates the simple net charge of the region. (B) The net charge of Ddx4 (red) and Ddx3x (orange) orthologues is shown relative to the net charge distribution of the human proteome (grey). Underflow and overflow binning for sequences with net charges <-50 and >50, respectively, was applied. (C) The transition temperature for Ddx4 orthologues (red) display a similar sensitivity to calcium (bold edged circles), whereas the Ddx3x orthologues (orange) are relatively unaffected. Error bars represent the standard deviation. (D) N- and C-terminal disordered regions of Ddx4 orthologues display a greater degree of charge patterning compared to the equivalent regions in Ddx3x orthologues. Kappa values were calculated using localCIDER (45) and indicate the degree of charge patterning. (E) Various factors can influence the phase separation propensity of a biomolecule. Fine tuning of dense and dilute phase properties can occur by modulating each of the individual properties.

Materials and Methods

Protein expression and purification

DNA sequences for Ddx4 and Bel constructs were generated by PCR and subcloned into pET SUMO vectors. Transformed BL-21 codon plus RIL *E. coli* cells were grown at 37°C to an optical density of 0.6-1 in terrific broth and induced with 0.5 mM IPTG. Protein expression was left to occur overnight at 22°C, 180 rpm. To reduce protein degradation during sonication and affinity purification, cell pellets were resuspended in 20 mM sodium phosphate, 10 mM imidazole, 6 M guanidinium hydrochloride (GdmCl), pH 7.4. Sonicate supernatants were loaded onto Ni-NTA agarose resin and incubated for >1 hour at 4°C. After washing with 20 mM sodium phosphate, 10 mM imidazole, pH 7.4, the bound SUMO-tag was removed by the protease ULP-1, and cleaved Ddx4 was eluted from the resin supernatant. The protein was further purified by size exclusion chromatography, using an elution buffer of 20 mM Tris, 300 mM NaCl, 5 mM TCEP, pH 8 at 22°C.

GST tagged protein constructs (Ddx3x, Ddx3y, Vasa, YFP) were generated by subcloning sequences of interest into a modified pETM-30 vector containing the pGEX-2T-TEV site and pProEx multiple cloning site. Transformed BL-21 codon plus RIL *E. coli* cells were grown at 37°C to an optical density of 0.6-1 in terrific broth and induced with 0.5 mM IPTG. Protein expression was left to occur for 4 hours at 37°C or overnight at 22°C. Cell pellets were typically resuspended in buffer containing 20 mM Tris pH 8 at 22-25°C, 300 mM NaCl, 2 mM DTT and EDTA-free protease inhibitor tablets (Roche). Sonicate supernatants were loaded onto GST-4B resin (Amersham) and incubated for >1 hour at 4°C. Resin was typically washed with 20 mM Tris pH 8, 1.5 M NaCl, 2 mM DTT and then exchanged into 20 mM Tris pH 8 at 22, 300 mM NaCl, 2 mM DTT, 2 mM EDTA. The GST-tag was removed by TEV protease, and cleaved protein was eluted from the resin supernatant. The protein was further purified by size exclusion chromatography, using an elution buffer of 20 mM Tris, 300 mM NaCl, 1 mM TCEP, pH 8 at 22-25°C.

Protein purity and identities were confirmed by SDS-PAGE and mass spectrometry, respectively.

HeLa Cell culture and transfection

HeLa cells were cultured as previously described (9, 26). Briefly, HeLa cells were grown on 22 mm diameter #1.5 glass coverslips (Agar Scientific) in growth media (high glucose DMEM (Gibco™) containing 10% FBS (Sigma)) at $37^{\circ}C$ and 5% CO_2. Protein constructs were expressed in HeLa cells from pcDNA 3.1+ (Invitrogen) plasmids by transient transfection using the TransIT®-LT1 Transfection Reagent (Mirus). Transfections used 0.5 – 1 µg plasmid DNA per coverslip and were carried out according to the manufacturer's instructions. Transfected cells were fixed approximately 24 hours after transfection.

Protein Sequences

Amino acid sequences for the constructs used in this work are shown below. Sequences correspond to the longest length constructs, with mutated regions shown in red and remnants from cloning in blue. Underlined residues indicate fluorophore sequences.

Ddx4^N (Uniprot: Q9NQI0; 1-238)

GAMGSMGDEDWEAEINPHMSSYVPIFEKDRYSGENGDNFNRTPASSSEMDDGPSRRDHF MKSGFASGRNFGNRDAGECNKRDNTSTMGGFGVGKSFGNRGFSNSRFEDGDSSGFWR ESSNDCEDNPTRNRGFSKRGGYRDGNNSEASGPYRRGGRGSFRGCRGGFGLGSPNNDL DPDECMQRTGGLFGSRRPVLSGTGNGDTSQSRSGSGSERGGYKGLNEEVITGSGKNSW KSEAEGGESSD

Ddx3x^N (Uniprot: Q9NQI0; 1-137)

GAMGSMSHVAVENALGLDQQFAGLDLNSSDNQSGGSTASKGRYIPPHLRNREATKGFYD KDSSGWSSSKDKDAYSSFGSRSDSRGKSSFFSDRGSGSRGRFDDRGRSDYDGIGSRGD RSGFGKFERGGNSRWCDKSDEDDWS

Ddx3y^{N} 135 (O15523; 1-135)

GAMGSMSHVVVKNDPELDQQLANLDLNSEKQSGGASTASKGRYIPPHLRNREASKGFHD

KDSSGWSCSKDKDAYSSFGSRDSRGKPGYFSERGSGSRGRFDDRGRSDYDGIGNRERP

GFGRFERSGHSRWCDKSVEDDWS

Vasa^{N} (P09052; 1-192)

GAMGSMSDDWDDEPIVDTRGARGGDWSDDEDTAKSFSGEAEGDGVGGSGGEGGGYQG

GNRDVFGRIGGGRGGGAGGYRGGNRDGGGFHGGRREGERDFRGGEGGFRGGQGGSR

GGQGGSRGGQGGFRGGEGGFRGRLYENEDGDERRGRLDREERGGERRGRLDREERG

GERGERGDGGFARRRRNEDDINNNNNIV

Bel^{N} (Q9VHP0; 1-252)

GAMGSMSNAINQNGTGLEQQVAGLDLNGGSADYSGPITSKTSTNSVTGGVYVPPHLRGG

GGNNNAADAESQGQGQGQGQGFDSRSGNPRQETRDPQQSRGGGGGEYRRGGGGGGGR

GFNRQSGDYGYGSGGGGRRGGGGGRFEDNYNGGEFDSRRGGDWNRSGGGGGGGRGF

GRGPSYRGGGGGSGSNLNEQTAEDGQAQQQQQPRNDRWQEPERPAGFDGSEGGQSA

GGNRSYNNRGERGGGGYNSRWKEGGGSNVDYT

Ddx4^{YFP}

MGDEDWEAEINPHMSSYVPIFEKDRYSGENGDNFNRTPASSSEMDDGPSRRDHFMKSGF

ASGRNFGNRDAGECNKRDNTSTMGGFGVGKSFGNRGFSNSRFEDGDSSGFWRESSND

CEDNPTRNRGFSKRGGYRDGNNSEASGPYRRGGRGSFRGCRGGFGLGSPNNDLDPDEC

MQRTGGLFGSRRPVLSGTGNGDTSQSRSGSGSERGGYKGLNEEVITGSGKNSWKSEAE

GGESSDMVSKGEELFTGVVPILVELDGDVNGHKFSVSGEGEGDATYGKLTLKFICTTGKLP

VPWPTLVTTFGYGLMCFARYPDHMKQHDFFKSAMPEGYVQERTIFFKDDGNYKTRAEVKF

EGDTLVNRIELKGIDFKEDGNILGHKLEYNYNSHNVYIMADKQKNGIKVNFKIRHNIEDGSVQ

LADHYQQNTPIGDGPVLLPDNHYLSYQSKLSKDPNEKRDHMVLLEFVTAAGITFSTYIPGFS

GSTRGNVFASVDTRKGKSTLNTAGFSSSQAPNPVDDESWD(GSGSG[tag])

Ddx4[CFP]

MGDEDWEAEINPHMSSYVPIFEKDRYSGENGDNFNRTPASSSEMDDGPSRRDHFMKSGF

ASGRNFGNRDAGECNKRDNTSTMGGFGVGKSFGNRGFSNSRFEDGDSSGFWRESSND

CEDNPTRNRGFSKRGGYRDGNNSEASGPYRRGGRGSFRGCRGGFGLGSPNNDLDPDEC

MQRTGGLFGSRRPVLSGTGNGDTSQSRSGSGSERGGYKGLNEEVITGSGKNSWKSEAE

GGESMVSKGEELFTGVVPILVELDGDVNGHKFSVSGEGEGDATYGKLTLKFICTTGKLPVP

WPTLVTTLTWGVQCFARYPDHMKQHDFFKSAMPEGYVQERTIFFKDDGNYKTRAEVKFE

GDTLVNRIELKGIDFKEDGNILGHKLEYNAISDNVYITADKQKNGIKANFKIRHNIEDGSVQLA

DHYQQNTPIGDGPVLLPDNHYLSTQSKLSKDPNEKRDHMVLLEFVTAAGITFSTYIPGFSGS

TRGNVFASVDTRKGKSTLNTAGFSSSQAPNPVDDESWD

YFP (mCitrine)

GAMGSMVSKGEELFTGVVPILVELDGDVNGHKFSVSGEGEGDATYGKLTLKFICTTGKLPV

PWPTLVTTFGYGLMCFARYPDHMKQHDFFKSAMPEGYVQERTIFFKDDGNYKTRAEVKFE

GDTLVNRIELKGIDFKEDGNILGHKLEYNYNSHNVYIMADKQKNGIKVNFKIRHNIEDGSVQL

ADHYQQNTPIGDGPVLLPDNHYLSYQSKLSKDPNEKRDHMVLLEFVTAAGIT

Buffers and reagents

Unless otherwise stated, in vitro experiments were performed in a pH 8 buffer containing 20

mM Tris, 150 mM NaCl and 5 mM TCEP. This was typically achieved through mixing protein

solutions (20 mM Tris, 300 mM NaCl, 5mM TCEP) with 20 mM Tris, 5 mM TCEP, which

reduced both the ionic strength and protein concentration of the stock solution and promoted

phase separation. For salt studies, 4x salt solutions were mixed with 2x buffer solutions (e.g.

40 mM $CaCl_2$ mixed with 40 mM Tris, 10 mM TCEP). This gave a final 2x salt solution in 1x

buffer that was mixed with the protein solution (e.g. providing final buffer conditions of 20

mM Tris, 150 mM NaCl, 10 mM $CaCl_2$, 5 mM TCEP). To improve the accuracy of the dilutions, all mixing steps outlined above were performed with a 1:1 volume ratio.

For Hela cell experiments involving treatment with salts, cells were grown in DMEM (ThermoFisher; 31966021) with 9 % FBS (Sigma; F9665).

Zeta potential

Zeta potential measurements were performed using a Zetasizer Nano (Malvern Pananalytical). Samples were prepared at 15 µM and filtered (0.22 µM) prior to taking the measurement. The mean zeta potential and standard error were calculated from 2-4 independently prepared sample replicates, with each replicate consisting of at least 3 estimates.

Net charge calculator

To calculate the net charge of each protein construct, the proportion of each ionisable group was calculated at each pH using the Henderson-Hasselbach equation and the following pKa values; C-term = 3.6, ASP = 4, GLU = 4.5, HIS = 6.4, N-term = 7.8, CYS = 8.14, TYR = 9.6, LYS = 10.4, ARG = 12.5. This was multiplied by the number and sign of each respective amino acid / ionisable group that was present in the construct, with the net charge determined from the sum of these values.

Transition temperature determination

Transition temperature measurements were typically performed as described previously (46). Briefly, 0.22 mm thick siliconized glass coverslips (Hampton Research), buffers and protein solutions were preheated on the heating block of a thermomixer. The ionic strength of the protein solution was diluted with buffer (typically 20 mM Tris, 5 mM TCEP, pH 8) containing various concentrations of different salts before transferring to the coverslip. The imaging chamber was sealed with 0.12 mm imaging spacers (Sigma) and a second

siliconized glass coverslip. Samples were transferred to a pre-heated Linkam PE120xy temperature-controlled imaging stage controlled with LinkSys software (Linkham) and imaged using a 10x differential interference contrast (DIC) objective on an Olympus BX43 microscope. Temperature ramps typically consisted of a 2°C/min reduction in temperature and were initiated at least 10°C above the transition temperature.

For analysis, twelve images of an isothermal sample were captured at the peak temperature of the ramp and used to calculate a baseline pixel intensity. Upon phase separation, condensate formation resulted in a change in observed pixel intensity. The transition temperature was then defined as the temperature at which the pixel intensity deviated by >10 standard deviations of the baseline intensity.

Confocal fluorescence microscopy of in vitro samples

To increase contrast through fluorescence imaging, the fluorescent molecules, Alexa 488 or mCitrine (YFP), were included in all samples at a final concentration of approximately 0.6 µM and 2 µM, respectively. Images were captured at room temperature using a Leica TCS-SP5 confocal fluorescence microscope and a 63x oil immersion objective. Samples were illuminated with a 488 nm (Alexa 488) or 514 nm (YFP) laser, with power and gain settings adjusted to give mean fluorescence intensity values of the dense phase of approximately 50-70% of the maximum 16-bit depth (~32,000-46,000 a.u.). Images were typically captured with settings of 256 x 256 pixels at ~ 98 x 98 x 98 nm (XYZ) resolution, 1400 hz and a line average of 2.

Phase separation was initiated by mixing proteins solutions with a buffer of lower ionic strength, as described above, and were left for 10 mins to promote droplet growth. Phase separated solutions were then transferred to a 0.22 mm thick siliconized glass coverslip (Hampton Research), before sealing with 0.12 mm imaging spacers (Sigma) and a second

siliconized glass coverslip. Samples were then left to equilibrate for approximately 50 minutes prior to imaging.

In vitro partitioning

Image analyses were performed using bespoke procedures in Mathematica 12. 3D image stacks of sessile droplets resting on a solid substrate were collected using laser scanning confocal fluorescence microscopy as above. In the positive z-direction, optical sectioning moved out of the solid substrate into the aqueous solution containing droplets. The xy slices containing the aqueous solution were identified by first measuring the change in pixel standard deviation, per slice, in z. The maxima of the change in standard deviation of pixel intensity in z was taken to approximate the position of the solid-aqueous interface. All images in z positions greater than this value plus 3 were carried forwards. A gaussian blur was then applied, using the "GaussianFilter" function with a kernel of radius 3, to the 3D image stack composed of the aqueous phase images. The blurred images were then binarized using the "Binarize" function with the default method of Otsu's algorithm. This generated a binary mask containing the condensed protein phase, whilst excluding the dilute protein phase. Dense phase intensity values were then extracted using the "ImageMeasurements" function from the original 3D image stack containing only the aqueous phase as the first argument, "MeanIntensity" as the second argument and an eroded version of the condensed phase mask (generated using the "Erosion" function"). Equivalently, dilute phase intensity values were extracted using the same procedure, except for the application of an eroded negative of the condensed phase mask to identify only the dilute phase. In both cases, the erosion ensured no edge effects caused by the blur of dilute phase voxels with dense phase voxels.

YFP typically generated little contrast between the dilute and dense phase, making automated droplet identification difficult. Mean pixel intensities where therefore determined from manually drawn regions of interest from at least five fields of view. Before calculating

the fluorescence intensity ratio, background dense and dilute phase intensities, determined from samples lacking a fluorophore, were subtracted.

Imaging fixed HeLa cells

HeLa cells expressing fluorescent proteins were grown on 22 mm diameter glass coverslips, washed twice with phosphate buffered saline (PBS) at 37°C and fixed with 4% paraformaldehyde (PFA) in PBS (Alfa Aesar) at 37°C, for 5 minutes. Cells were then washed three times with PBS to remove excess PFA with the first wash only containing Hoechst 33342 dye at 2 μM. Cells were incubated for 5-10 minutes in the wash solution at each step. Coverslips were mounted on microscope slides (Fisher Scientific™) using Immu-Mount (Thermo Scientific™ Shandon™) mounting medium.

Cells were imaged on an Olympus FV1000 Laser Scanning Microscope based on an Olympus IX81 inverted microscope with a motorised stage, and equipped with an Olympus PLAPON60XOSC2 (NA 1.4) oil immersion objective. Hoechst was excited with a solid state 405 nm laser and YFP (mCitrine) was excited with an argon 515 nm laser. Hoechst fluorescence was collected between (420 - 435 nm) and YFP fluorescence was collected between (530 - 650 nm). DIC images were collected using illumination from the 515 nm laser.

Unless otherwise stated, imaging data were collected as stacks of 86 Z-slices (256 x 256 pixels (xy), 0.1 µm spacing (z), 2 µs pixel^{-1} scanning speed, 12 bit depth, 2 x line averaging) for each channel. In all cases the YFP stack was collected before the Hoechst channel stack was collected. Image analysis was performed using Wolfram Mathematica (Wolfram Research, Inc., Mathematica, Version 12.0, Champaign, IL (2019)) and Fiji (47). Figures were prepared using Fiji and Omero Figure (48).

In cell determination of saturation concentration and partitioning

Imaging data was collected with identical laser power and detector sensitivity so that fluorescence intensities across difference samples were directly comparable. Image analyses to extract intensities for Ddx4YFP droplets and the nucleoplasm (excluding nucleoli) were performed using bespoke procedures in Mathematica 12.

To the YFP image stack, the "GaussianFilter" function was applied with a kernel of radius 3. This blurred 3D image was then binarized, using the Binarize function with the default options, to obtain a binary mask of the voxels containing Ddx4 droplets. When utilised for the extraction of pixel intensities, the Ddx4 droplets mask was subjected to an "Erosion" of 3 voxels. To the DAPI image stack, the "GaussianFilter" function was applied with a kernel of radius 10, followed by the "Binarize" function with the default options, generating a binary mask of the nucleus. This binary image was then multiplied by the negative of the mask of the condensed protein phase, generating a binary mask of the nucleus, excluding Ddx4 droplets. The resultant image was then subjected to an "Erosion" of 5 voxels, generating a binary mask of the nucleus, excluding Ddx4 droplets. This mask was then multiplied by the blurred YFP image, generating an image containing only the nucleus, whilst excluding Ddx4 droplets. The "FindThreshold" function was applied to all non-zero voxel values, to obtain the intensity value separating nucleolar from nucleoplasm voxel intensity. This threshold was to set the threshold of the "Binarize" function applied to the blurred YFP image containing only the nucleus and excluding Ddx4 droplets. This generated a binary image mask containing only the nucleoplasm. A binary image of the nucleoli was then generated by multiplying the negative of the nucleoplasm binary mask by the binary mask containing the nucleus and excluding Ddx4 droplets. This binary image was then subjected to an "Erosion" of 2 voxels, generating a binary mask containing only voxels from the nucleoli. The "ComponentMeasurements" function was then applied to the YFP image stack, using the corresponding masks to extract "MeanIntensity" voxel values for the corresponding regions of the image stack. Before calculating the fluorescence intensity ratios, background intensity, determined from fluorescence in extracellular regions of each sample, were subtracted.

Real-time droplet imaging

Ddx4^N 1-236 was allowed to phase separate by mixing in a 1:1 volume ratio with 20 mM Tris, 5 mM TCEP, 1.2 μM Alexa 488 (final buffer composition of 20 mM Tris, 150 mM NaCl, 5 mM TCEP, 0.6 µM Alexa 488, pH 8 at 22°C), before transferring 2 µL to a siliconized glass coverslip. To prevent evaporation during the course of the experiment, 10 µL of mineral oil was added on top of the beaded Ddx4 solution, forming a seal. To rapidly collect XYZ confocal images (approximately 15s per stack), settings of 128 x 128 pixels at ~300 x 300 x 300 nm (XYZ) resolution, 1400 hz and line average of 2 were used.

Solutions containing CaCl$_2$ and EDTA were generated by mixing a 4x stock with Ddx4^N 1-236. For example, 20 mM Tris, 5 mM TCEP, pH 8, 40 mM CaCl$_2$, 1.2 µM Alexa 488 was mixed with Ddx4^N 1-236 giving final conditions of Ddx4N 1-236 in 20 mM Tris, 150 mM NaCl, 5 mM TCEP, pH 8, 20 mM CaCl$_2$, 0.6 µM Alexa 488. Using a 10 µL pipette tip to pierce the mineral oil film, 2 µL of this solution was then added to the solution being imaged. This ensured that all components except the additive (e.g. CaCl$_2$) remained at the same concentration in the sample. Upon removing the pipette tip, the mineral oil reformed the seal, preventing any water loss through evaporation.

Live-cell imaging

Approximately 17,500 HeLa cells were seeded in 3.5 cm glass bottomed imaging dishes (Imbidi), incubated overnight at 37°C and 5% CO$_2$ in DMEM + 10% FBS and transfected with 1 µg of DNA. Expression was allowed to proceed over a 24-hour incubation period at 37°C. The cell permeant calcium sensitive dye, Fluo 5F was reconstituted in DMSO to a concentration of 1 mM. Prior to imaging, 2 µL of Fluo 5F was added to each dish (1 µM final concentration). After incubation at 37°C and 5% CO$_2$ for approximately 30 mins to allow cellular uptake of Fluo 5F, excess dye was removed by exchanging the growth media. Cells were then imaged using a Delta Vision Elite microscope with an Olympus 60x (1.42 NA) oil

immersion objective and an Evolve 512 EMCCD camera (Photometrics). Ddx4^{CFP} and Fluo 5f were illuminated at 438 nm and 513 nm, and CFP and YFP emission filters were used with exposure times of 5 ms and 1 s, respectively. Images were captured using Resolve3D softWoRx-Acquire Version (6.5.2 Release RC1).

Flow cytometry

HeLa cells were grown in 15 cm plates to a confluency of approximately 50% and transfected with 10 µg of DNA. Expression was allowed to proceed over a 24-hour incubation period at 37°C and 5% CO_2, after which cells had typically reached a confluency of 70-80%. Cells were then dissociated using trypsin, pelleted and resuspended in PBS. To ensure differences in transfection efficiencies and passage number were not conflated with differences between salt conditions, resuspended cells from the same plate were split into different tubes. Cells were then pelleted and resuspended 20 mM Hepes, 137 mM NaCl, 2.7 mM KCl, pH 7.4 at 37°C, with or without additional salt (e.g. 20 mM Hepes, 137 mM NaCl, 2.7 mM KCl, 10 mM $CaCl_2$). Hepes was chosen at this stage to prevent phosphate precipitation by calcium. Cells were pelleted and resuspended again before incubating at 37°C and 5% CO_2 for 10 mins. Fixation was achieved by resuspending pelleted cells in PBS with 4% paraformaldehyde and incubating at room temperature for 10 mins, before washing cells with PBS. To concentrate cells for flow cytometry, cells were pelleted and resuspended in 100-200 µL of PBS. Cell data was collected by passing cells through an Amnis Imagestream flow cytometer. Typically, data from 100,000 cells were collected from each experimental replicate.

To identify cells with Ddx4 condensates, two parameters were used. Firstly, as formation of Ddx4 condensates occurs in a protein concentration dependent manner, we identified cells with high fluorescence intensity levels, which indicated high expression of the YFP-tagged Ddx4 construct. Secondly, the difference in protein concentration between the dense and dilute phases results in Ddx4 condensates having significantly higher fluorescence intensity

than the surrounding dilute phase. We reasoned that cells with high fluorescence contrast would therefore be more likely to have condensates, whereas cells with high concentrations of YFP-tagged Ddx4 but no condensates would have a more uniform fluorescence intensity and lower contrast. By plotting fluorescence intensity against fluorescence contrast, a population of cells with high intensity and high contrast could clearly be distinguished (Figure S2). Upon investigating images of these cells captured by the Imagestream cytometer, it appeared that these cells contained condensates. Furthermore, this population of cells was not present in cells expressing only YFP, indicating that these cells contained condensates composed of Ddx4. To count cells within this population, a boundary was drawn. This reduced the number of cells from the initial 100,000 to approximately 1000. Cells within this boundary were then manually inspected to remove false positives and ensure that condensate-like features could be identified. At least three experiments were performed for each salt condition.

Sequence analysis

We obtained amino acid sequences for all SwissProt reviewed human genes (20,359 entries at the time of download) from UniProt (49). Net Charge was computed as follows: amino acids Arginine and Lysine each contributed a charge of +1 and Aspartic Acid and Glutamic Acid each contributed a charge of -1. Kappa was calculated using localCIDER (45).

Alignment of orthologous Ddx4 and Ddx3x sequences was performed in Jalview (50) using the Muscle algorithm with default settings. Boundaries for protein domains (N and C-terminal IDRs and the central helicase domains) were determined from alignment of all orthologous sequences.

Organism	UniProtKB Entry	UniProtKB Entry name	N-term (amino acids)	Helicase domain (amino acids)	C-term (amino acids)
human	Q9NQI0	DDX4_HUMAN	1-245	246-676	677-724
human	O00571	DDX3X_HUMAN	1-135	136-576	577-662
mouse	Q61496	DDX4_MOUSE	1-218	219-649	650-702
mouse	Q62167	DDX3X_MOUSE	1-135	136-576	577-662
clawed frog	Q91372	DDX4_XENLA	1-231	232-662	663-700
clawed frog	P24346	DDX3_XENLA	1-176	177-617	618-697
zebrafish	O42107	O42107_DANRE	1-234	235-665	666-716
zebrafish	B0S6P6	B0S6P6_DANRE	1-178	179-624	625-709
fruit fly	P09052	VASA1_DROME	1-201	202-625	626-661
fruit fly	Q9VHP0	DDX3_DROME	1-250	251-694	695-798
flat worm	P34689	GLH1_CAEEL	1-275	276-740	741-763
flat worm	D0PV95	DDX3_CAEEL	1-186	187-627	628-708

Table 1. Gene names and domain boundaries used to calculate net charges displayed in Figure 4.

Supplementary Figure Legends

Figure S1. Phase diagrams for Ddx4^N constructs.

(A) Ddx4^N phase diagrams. Estimated rounded integer charges for the constructs are -3, -4, -5 and -6 for 1-229, 1-231, 1-234 and 1-236, respectively. Lines illustrate the fit to a Flory-Huggins model, as described previously. (B) Enthalpy and Entropy contributions to mixing, as determined from the Flory-Huggins fits. Data extracted for the 3.3 mM CaCl$_2$ phase diagram in Figure 3D is shown in red.
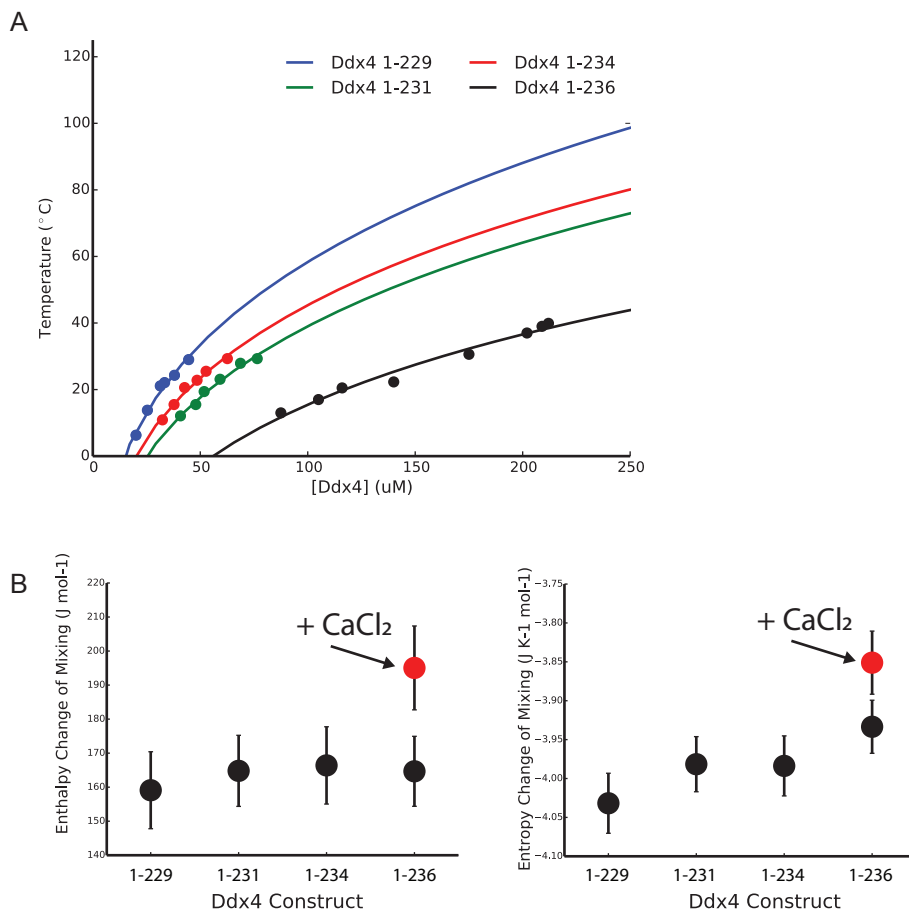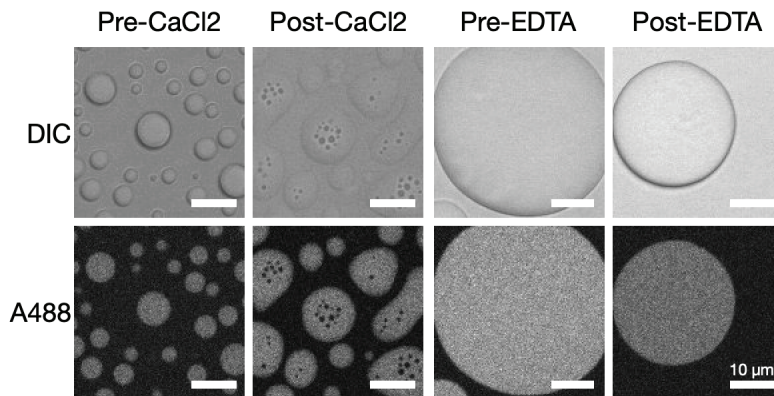
Figure S1

A

B

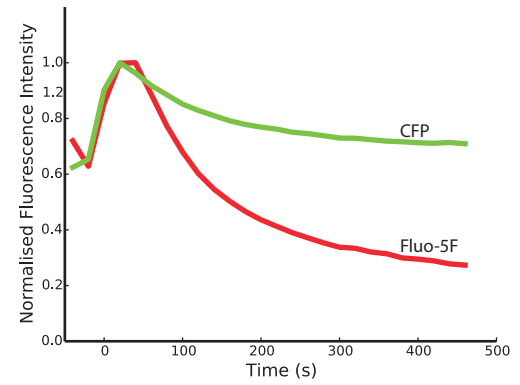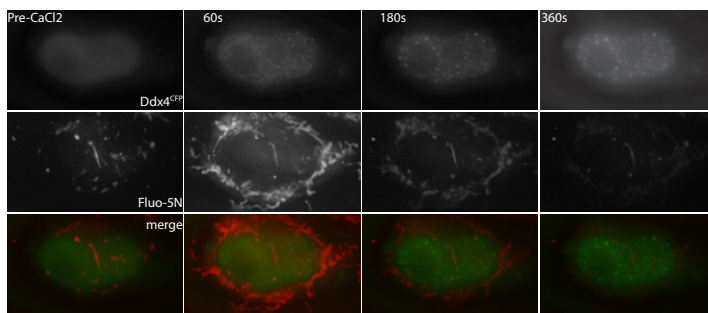Figure S2. Calcium impacts Ddx4 condensates in vitro and in cells.

(A) Time-lapse confocal fluorescence imaging of Ddx4^{YFP}(-11) droplets in response to 10 mM CaCl$_2$ addition and chelation by EDTA. Scale bar 10 μm. (B) Images (left) and time points (right) from live cell imaging of HeLa cells containing the calcium sensitive dye (Fluo 5F) and transiently expressing Ddx4^{CFP}. The quoted times indicate the time of image acquisition after addition of 10 mM CaCl$_2$ to the growth media. Mean fluorescence intensity in the CFP (Ddx4^{CFP}; green) and Fluo 5F (red) channels is shown. (C) Data from Flow cytometry of HeLa cells transiently expressing Ddx4^{YFP}(-11) (left) or YFP (right). A population of cells containing Ddx4^{YFP} condensates could be identified due to their high intensity and contrast. This population was not present in cells expressing only YFP. Representative images of cells in this region are indicted in inset images, with green arrows identifying the location of the cell on the intensity vs contrast plot. Droplets can be identified in cells expressing Ddx4^{YFP}(-11) that occur in this high intensity and contrast region. Data points represent a total of 10,000 cells, with approximately 1-2% occurring in the high intensity and contrast region for Ddx4^{YFP}(-11).

Figure S2

A

B

C